Supporting information

Structurally Tailored Nanocomposite Sorbent Enabling High-Energy-Density Thermochemical Storage in E-Thermal Banks for Electric Vehicle Applications

Waseem Aftab, Muhammad Khurram, Qiqiu Huang, Dacheng Li, Muhammad Maqbool, Jiatong Jiang, Yongliang Li**

Birmingham Centre for Energy Storage (BCES) & School of Chemical Engineering, University of Birmingham, Birmingham B15 2TT, United Kingdom

* corresponding author: Waseem Aftab (w.aftab@bham.ac.uk) and Yongliang Li (y.li.1@bham.ac.uk)

Materials and Methods

Synthesis of Graphene Oxide (GO)

GO was synthesized from natural graphite powder (325 mesh) using a modified Hummers' method. Briefly, 3.0 g of graphite was added to 70 mL of concentrated sulfuric acid under stirring at room temperature. Then, 1.5 g of sodium nitrate was added, and the mixture was cooled to 0 °C. Under vigorous stirring, 9 g of potassium permanganate was slowly added while maintaining the suspension temperature below 20 °C. The reaction mixture was subsequently transferred to a 40 °C water bath for 30 minutes, resulting in a thick paste. Afterward, 140 mL of water was added, and the mixture was stirred for an additional 15 minutes. This was followed by the addition of 500 mL of water and the slow addition of 20 mL of 30% hydrogen peroxide (H_2O_2), turning the solution colour from brown to yellow. The product was filtered and washed with 250 mL of 1:10 hydrochloric acid (HCl) aqueous solution to remove metal ions, followed by repeated washing with water and centrifugation to eliminate residual acid. The resulting solid was dispersed in water via ultrasonication for 1 hour to obtain

a GO aqueous dispersion. The brown dispersion was centrifuged at 4000 rpm for 30 minutes to remove any remaining aggregates.

Fabrication of GAS and $CaCl_2$@GAS Composite Sorbent

To prepare the GO ink, 0.25 g of a 3 wt.% $CaCl_2$ aqueous solution was added to 10 mL of a GO dispersion (12 mg/mL) and mixed thoroughly using a vortex mixer. The mixture was then left to rest for 12 hours to ensure uniform distribution of metal ions. The resulting ink was subsequently wet-spun into a coagulation bath containing 3 wt.% $CaCl_2$ in a 1:5 (v/v) ethanol–water solution, using a nozzle with the desired diameter. The resulting GO spheres were sealed in a 500 mL Teflon-lined autoclave and subjected to hydrothermal reduction at 180 °C for 12 hours. After natural cooling to room temperature, the GO hydrogel spheres were thoroughly washed with water several times to completely remove ethanol. The reduced GO hydrogel spheres were then frozen in hexane cooled by liquid nitrogen and subsequently freeze-dried to obtain graphene aerogel spheres (GAS). To load $CaCl_2$, the GAS spheres were immersed in a 20 wt.% $CaCl_2$ solution, and vacuum was applied to ensure complete infiltration of the salt solution into the pores of the GAS. The $CaCl_2$@GAS composites were then washed several times with water to remove surface salt and dried at 100 °C.

Characterization

The morphology and elemental composition of the materials were analyzed by scanning electron microscopy (SEM) using a Hitachi TM3030 microscope equipped with an energy-dispersive X-ray spectrometer (EDX; QUANTAX 70 Xflash® 430-H, Bruker). The measurements were performed in high vacuum mode at an accelerating voltage of 15 kV. Samples were dried and coated with a 5–10 nm layer of gold using a Q150R ES Plus rotary-pumped coater (Quorum) prior to analysis.

X-ray tomography (XRT) measurements were carried out using a Skyscan 2211 system (Bruker, USA) to investigate the internal and morphological structure of $CaCl_2$@GAS. Scans were conducted at 100 kVp, 200 μA, and 250 ms exposure time using a CCD detector. Images were recorded with a rotation step of 0.2° and an averaging of six frames per position. Reconstruction of 2D and 3D structures was performed using Bruker's XRT R-con software. While scanning parameters were kept constant across all samples, alignment, ring artifact correction, and beam-hardening adjustments were applied for optimal accuracy.

Crystal structure was determined by X-ray diffraction (XRD) using a Bruker D8 Advance diffractometer in Bragg–Brentano geometry (θ–2θ) with Cu $K\alpha_1$ radiation. Data were collected in the 2θ range of 10°–90°, with a step size of 0.02° and a counting time of 0.5 seconds per step. Variable-temperature XRD was performed with a heating rate of 5 °C/min.

Porous characteristics were evaluated via nitrogen adsorption–desorption isotherms using a TriStar II Plus surface area and porosity analyzer (Micromeritics). Samples were degassed under vacuum at 150 °C overnight to remove moisture. Measurements were carried out at −196 °C in liquid nitrogen. Surface area and pore size distributions were calculated using the Brunauer–Emmett–Teller (BET) method and the density functional theory (DFT) model in the pore range of 2 to ~100 nm.

Dynamic water sorption isotherms of the sorbents were obtained using a Dynamic Vapor Sorption (DVS) system (Resolution and Advantage models) at fixed and variable relative humidities (RH) ranging from 0% to 90%. The water sorption–desorption performance and corresponding enthalpy of the $CaCl_2$@GAS composite was further investigated using a thermogravimetric analyzer (STA 449C, Netzsch), equipped with a moisture humidity generator (MHG 32, ProUmid). Prior to each test, the samples were dried in an oven at 130 °C.

Sorption experiments were conducted at 25 °C under different RH conditions (60%–90%), followed by desorption at 130 °C.

Real-time MW-assisted thermochemical charging was conducted using a Milestone Flexi-wave MW generator coupled with a weighing balance and an infrared (IR) temperature sensor, enabling continuous tracking of mass loss and temperature evolution under fixed-power irradiation.

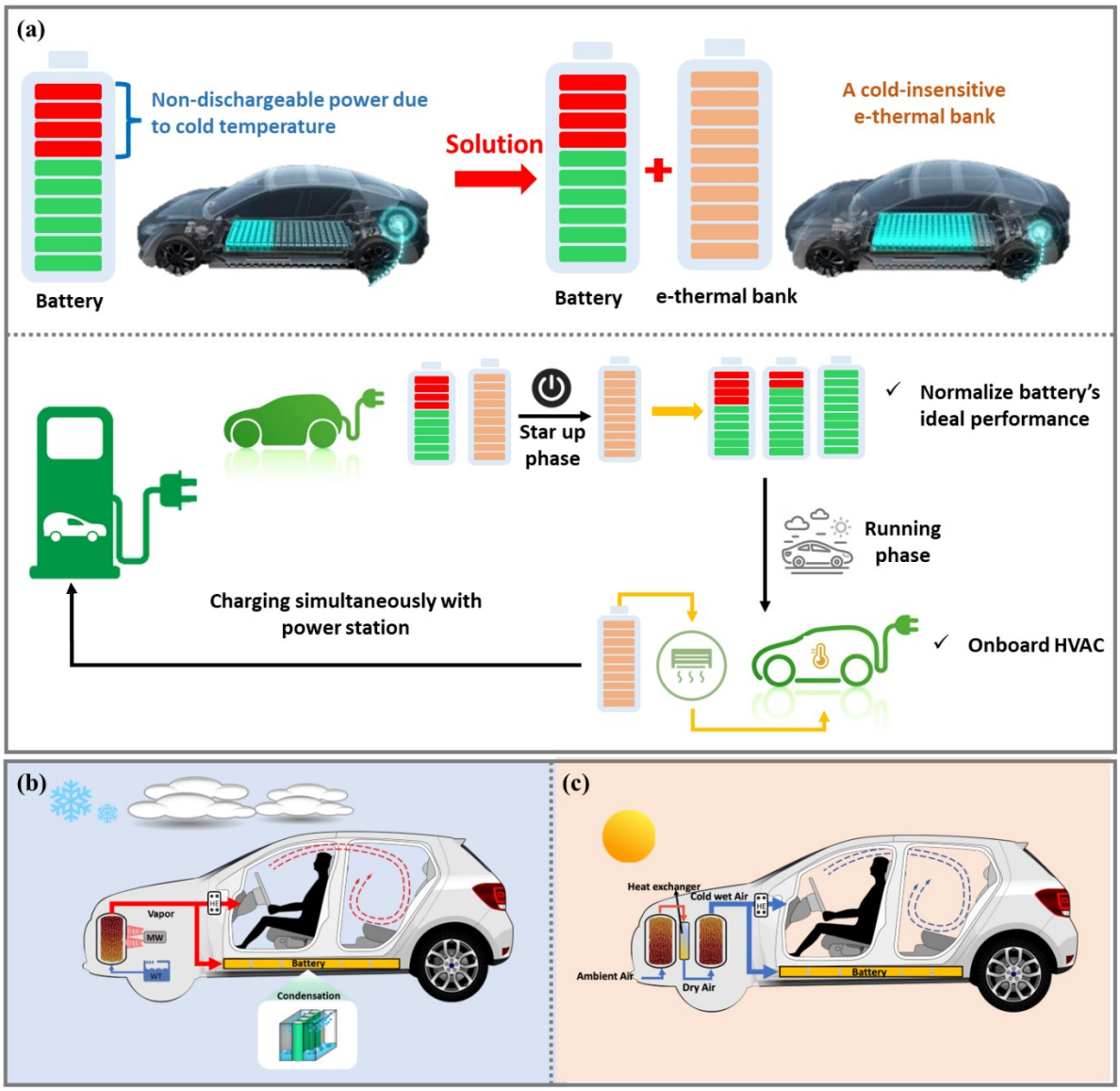

Figure S1. Concept and operating principles of the e-thermal bank. (a) Schematic illustration highlighting the poor performance of EVs batteries in cold climates and the

potential improvement by integrating an e-thermal bank, which can also serve onboard HVAC needs. Operating principle of the e-thermal bank during winter (b) and summer (c) conditions. The proposed TCS-integrated e-thermal bank can be directly charged using electricity (microwaves, MW) at charging stations without requiring additional infrastructure and consume little battery power during cruising. Additionally, the proposed e-thermal bank can be integrated with the battery thermal management (BTM) system to achieve a synergistic effect, effectively minimizing capacity loss under extreme environmental conditions. In charging process, electricity powers a MW generator, enabling energy-efficient, rapid, uniform, and volumetric heating to drive the desorption process. During desorption, the released sorbate (warm) can either pass through a heat exchanger (open system) or condense (closed system), thereby releasing condensation heat. This thermal energy can be repurposed for preconditioning electric battery packs, which typically require an energy-intensive warming process during fast charging in cold climates.[1-3] This dual functional of e-thermal bank offers multiple advantages: in cold conditions, it facilitates battery preconditioning, while in hot climates, it enhances battery heat recovery.[4, 5] This recovered heat can accelerate the desorption process during charging (alongside MW power) and be utilized for evaporative cooling while cruising, thereby converting waste heat into useful cooling. This multifunctionality not only improves battery cooling efficiency but also reduces overall energy consumption. During discharging, the onboard e-thermal bank can provide heating or cooling through sorption or evaporation. In an open system, ambient air is used directly, whereas in a closed system, a minimal amount of input energy may be required to achieve the desired thermal output.

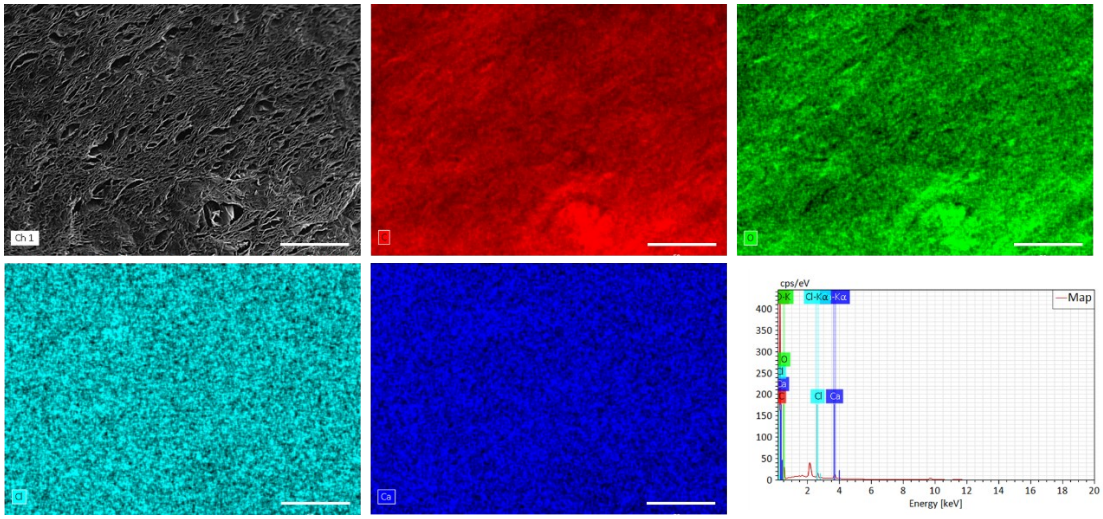

Figure S2. SEM image of GAS and corresponding elemental mapping. The scale bar is 50 μm.

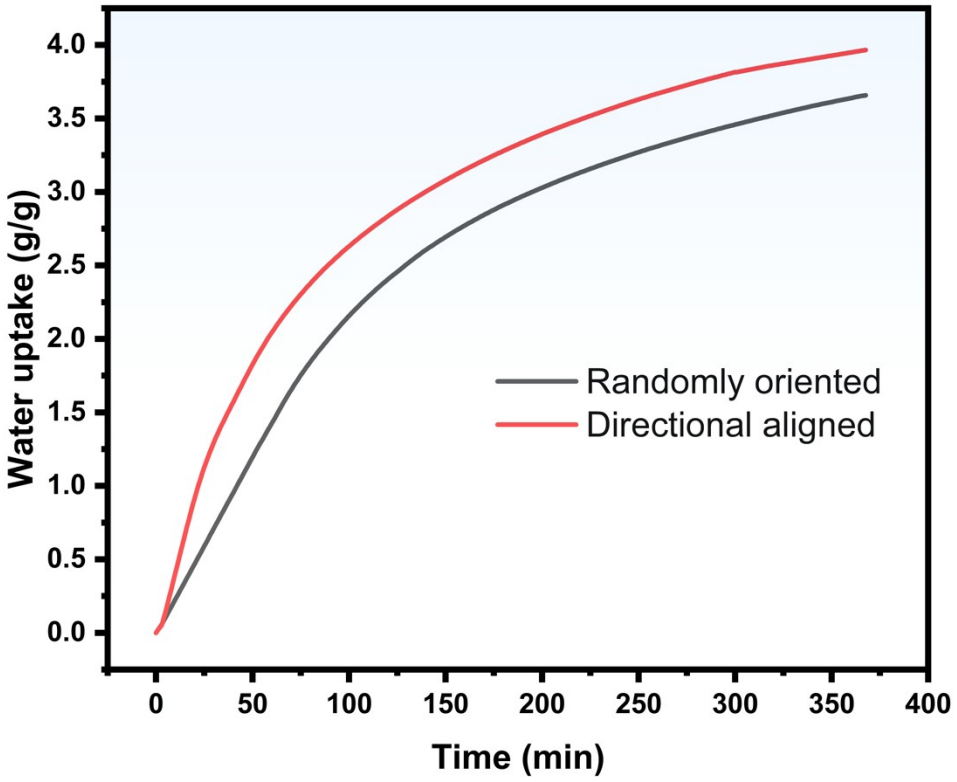

Figure S3. Sorption isotherms of randomly oriented and directionally aligned $CaCl_2$@GAS structures measured at 25 °C and 90% RH.

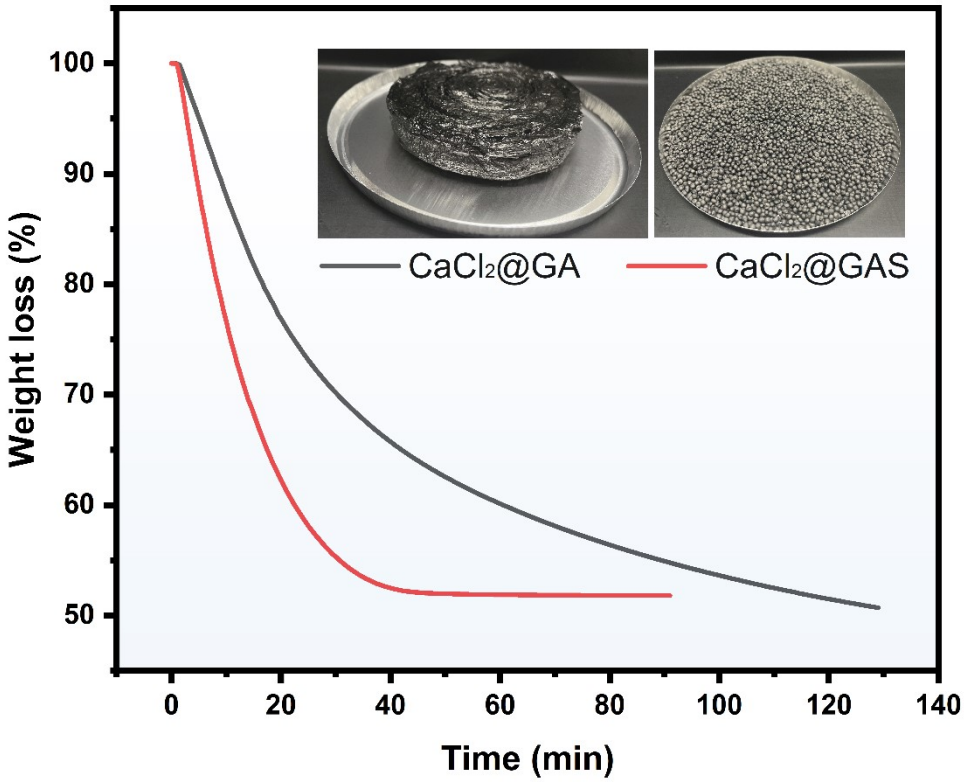

Figure S4. Comparative desorption performance of monolithic and spherical composite sorbents at 150 °C, following overnight sorption under ambient conditions (~40% RH).

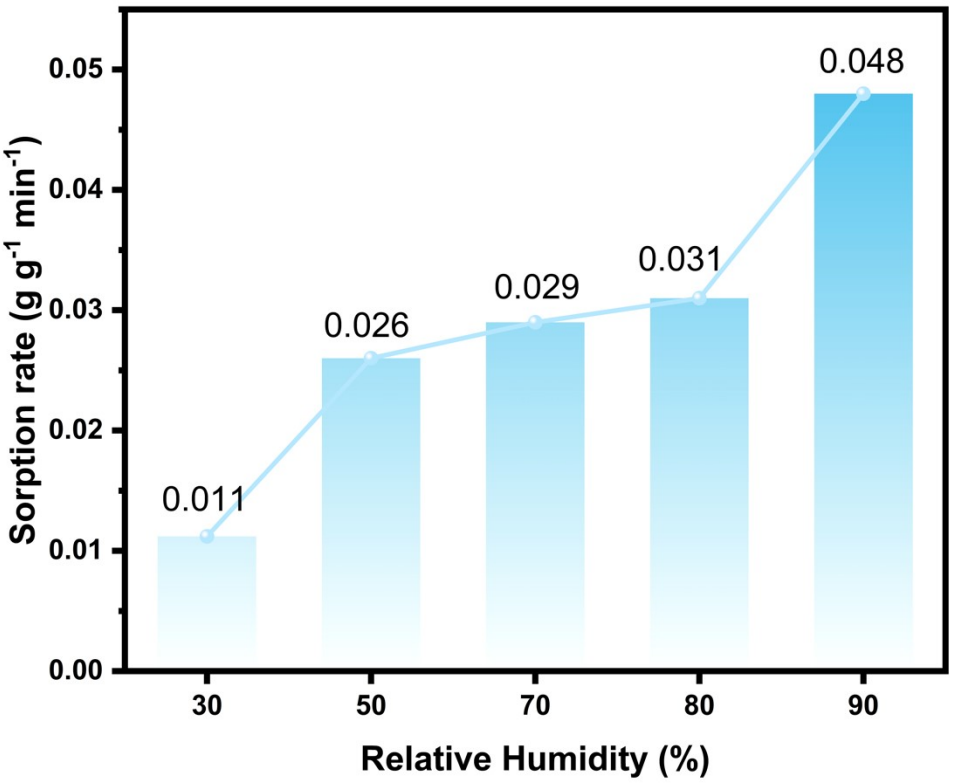

Figure S5. Maximum water sorption rate of $CaCl_2$@GAS as a function of RH. Note that the sorption rate is highly dependent on sample mass; the values presented here are based on measurements using a few milligrams of sample in the DVS system.

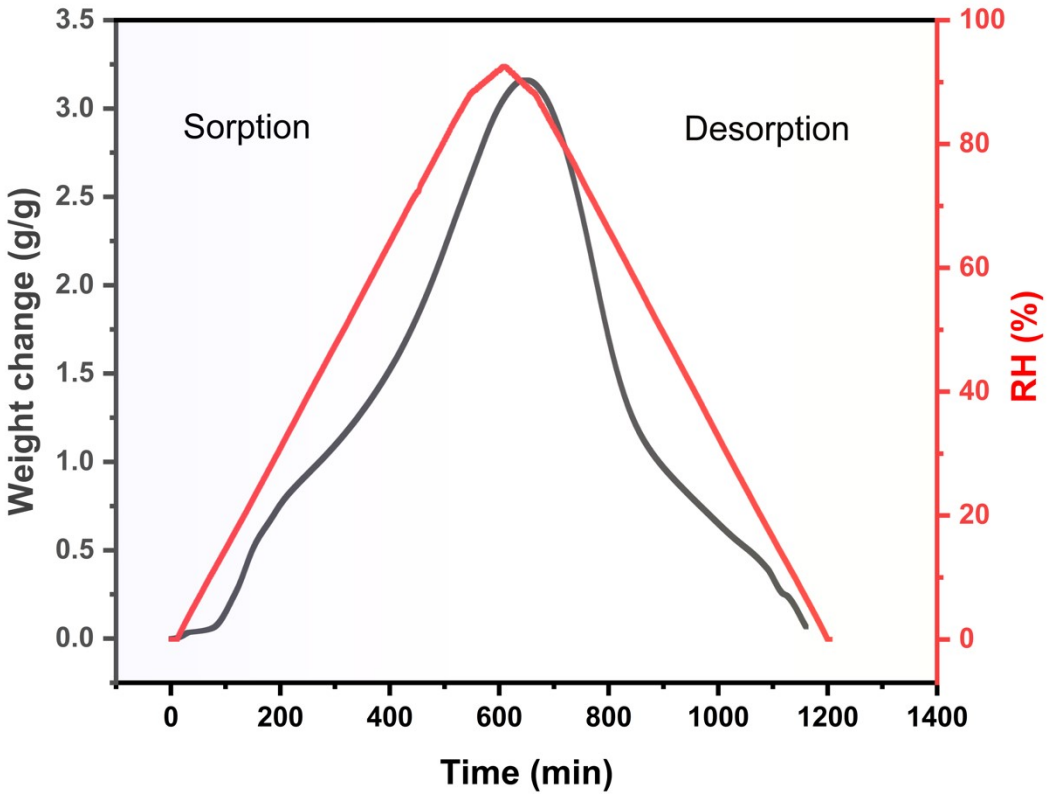

Figure S6. Reversible water sorption/desorption isotherms of $CaCl_2$@GAS measured under varying RH conditions, demonstrating the material's sorption reversibility.

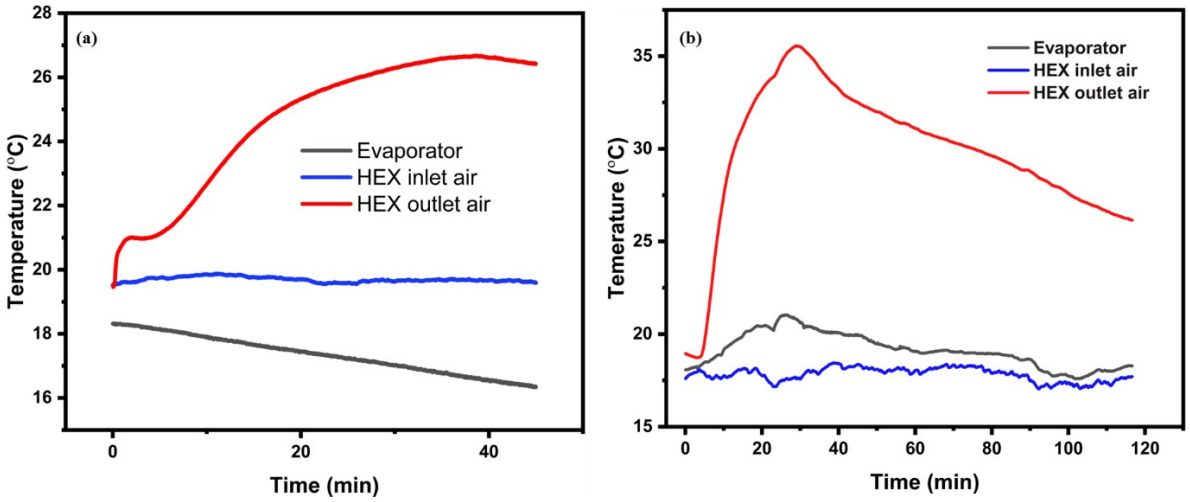

Figure S7. Performance of the close system at an air flow rate of 2L/min: (a) operation without a heated evaporator and (b) with a heated evaporator. Notably, even when the evaporator temperature is maintained by heating, the outlet air temperature gradually decreases due to the decreasing ammonia concentration in the ammonia–water solution.

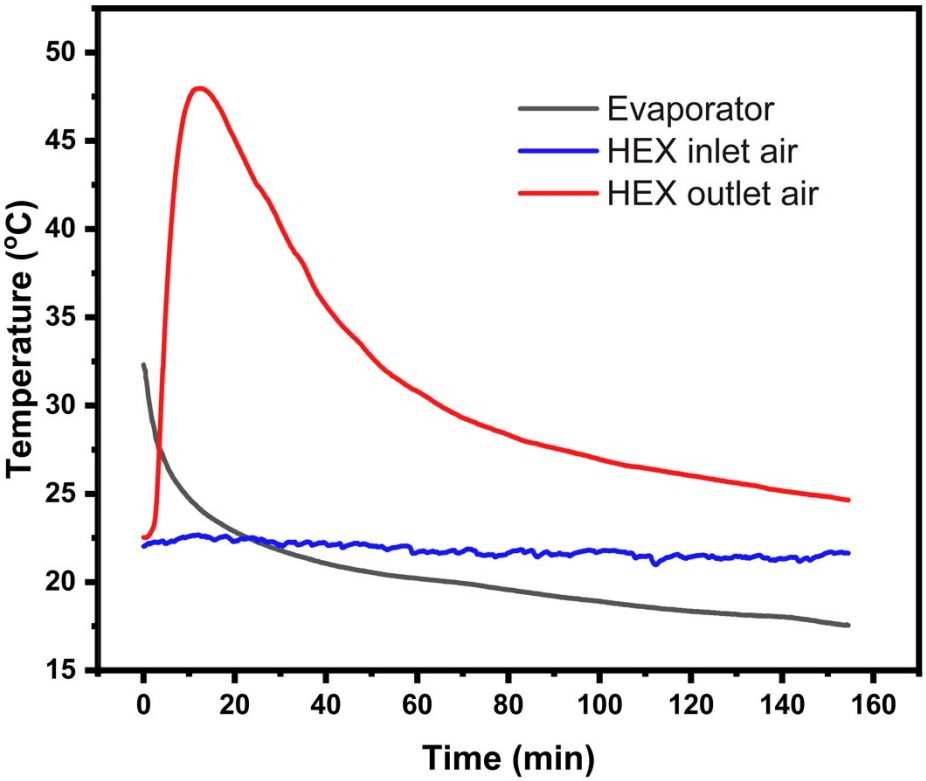

Figure S8. The temperature drop performance of the evaporator during closed cycle operation.

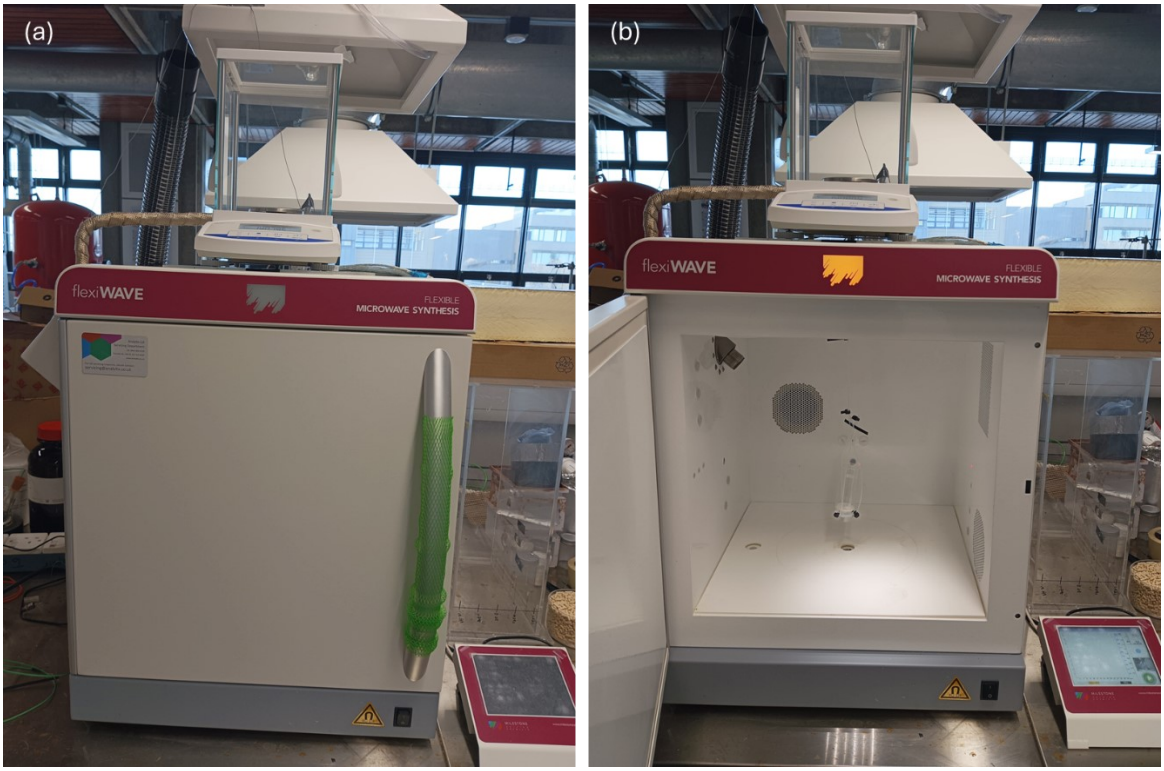

Figure S9. Photograph of the weight-balance–integrated FlexiWave microwave (MW) generator used to investigate the MW-driven desorption process: (a) exterior view; (b) interior view.

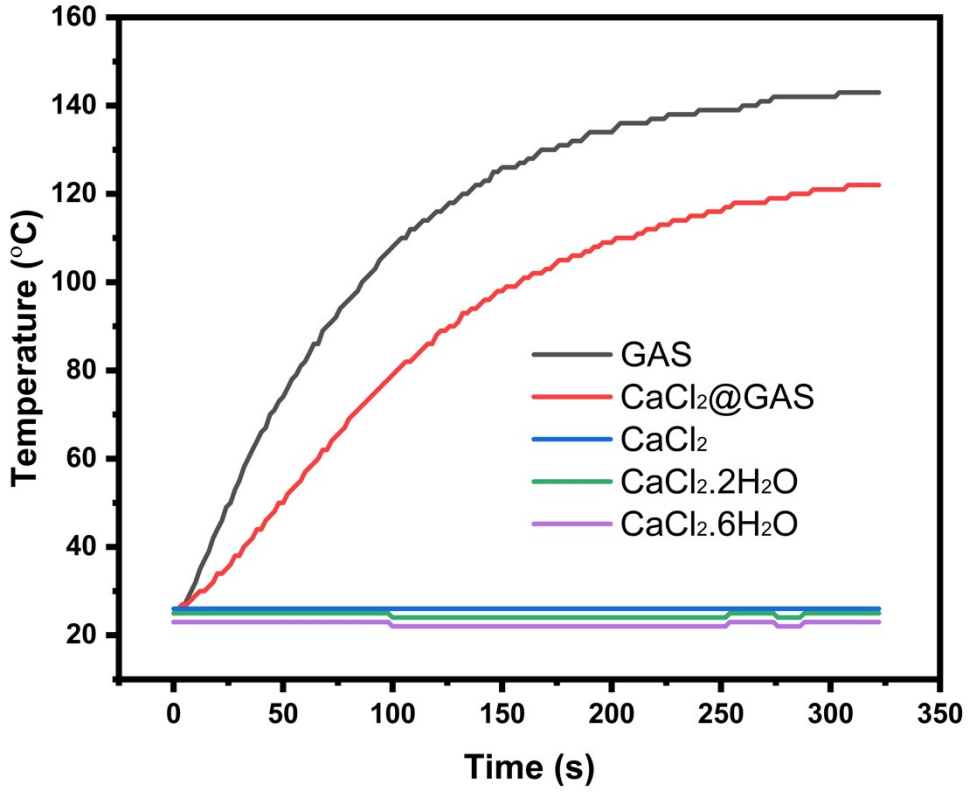

Figure S10. Temperature evolution of different materials during 50 W MW heating.

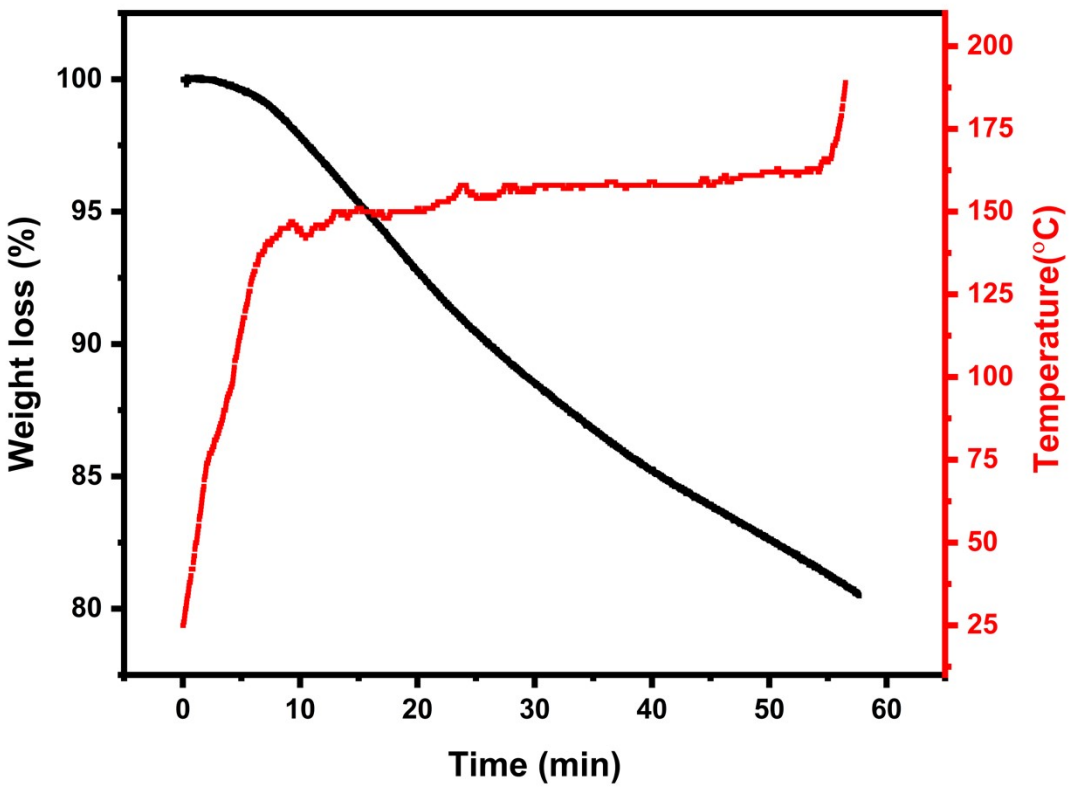

Figure S11. Temperature evolution and corresponding weight loss curves of melted $CaCl_2 \cdot 6H_2O$ under 100 W MW power with a sample weight of 60 g. The sample is not fully dehydrated even at temperatures reaching 180 °C, due to the low evaporation rate associated with liquid-phase water removal.

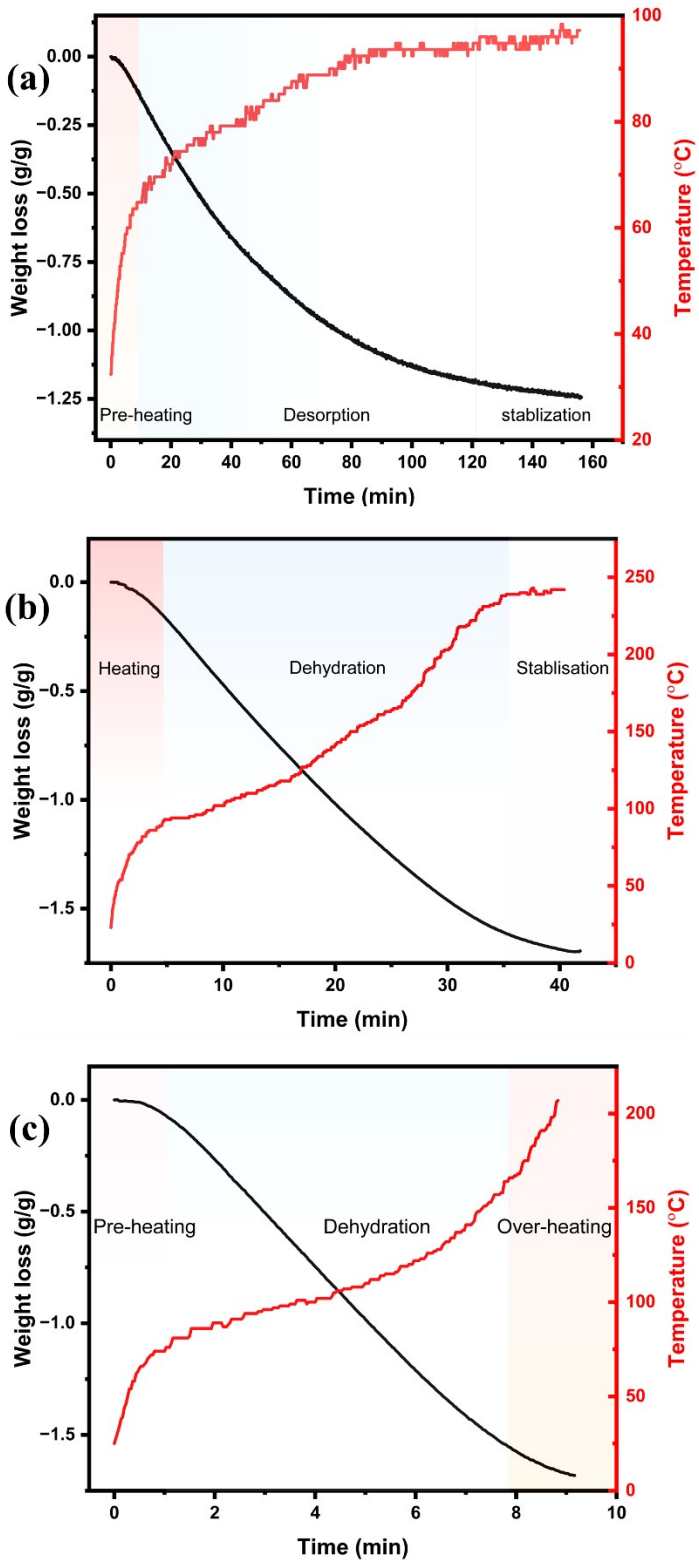

Figure S12. Time–temperature evolution and corresponding weight loss curves of $CaCl_2$@GAS under MW heating at different power levels: (a) 50 W, (b) 75 W, and (c) 100 W.

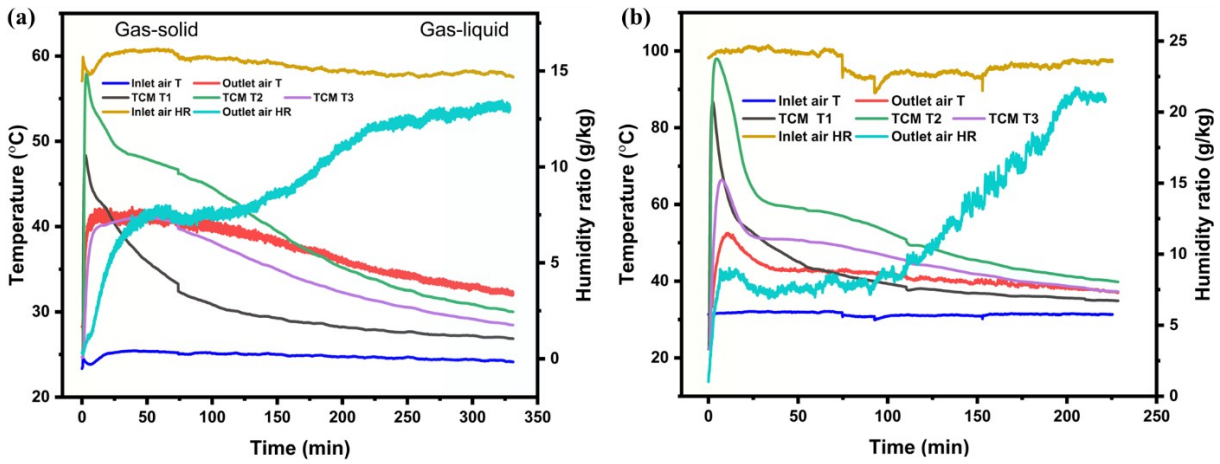

Figure 13. Temperature and humidity evolution during the discharging process at a flow rate of 20 SL/min: (a) inlet air temperature of 25 °C; (b) inlet air temperature of 30 °C.

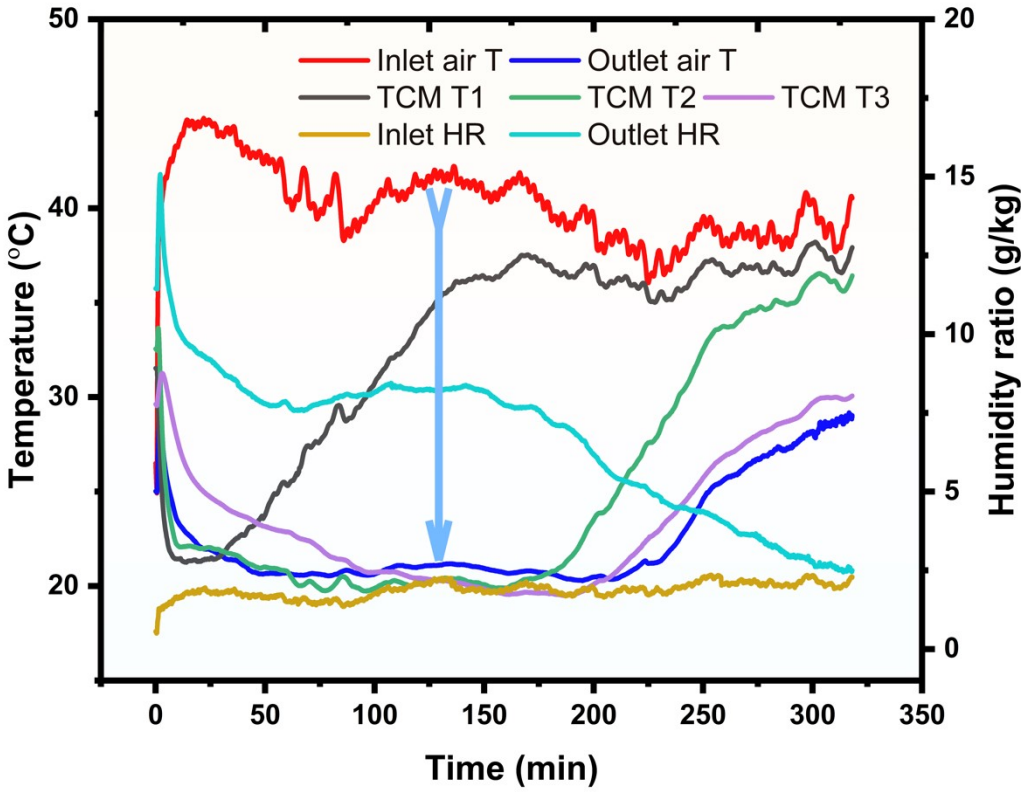

Figure S14. Temperature and humidity evolution during the evaporative cooling process at a flow rate of 20 SL/min, with an inlet air temperature of approximately 40 °C.

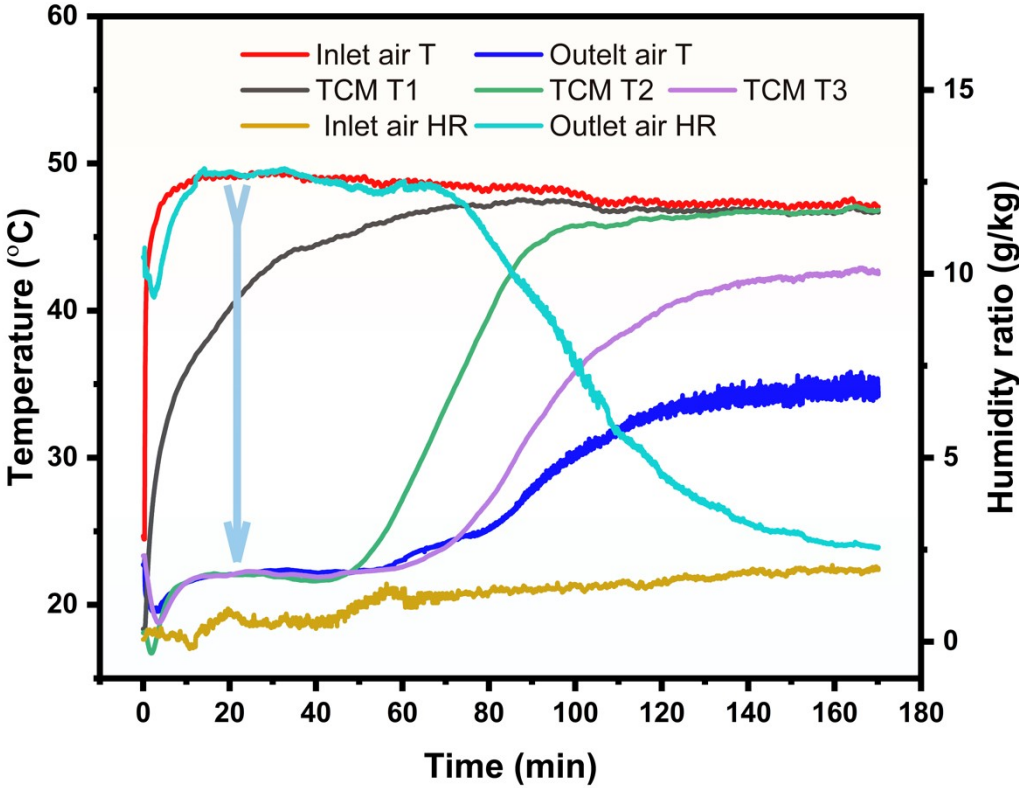

Figure S15. Temperature and humidity evolution during the evaporative cooling process at a flow rate of 30 SL/min, with an inlet air temperature of approximately 50 °C.

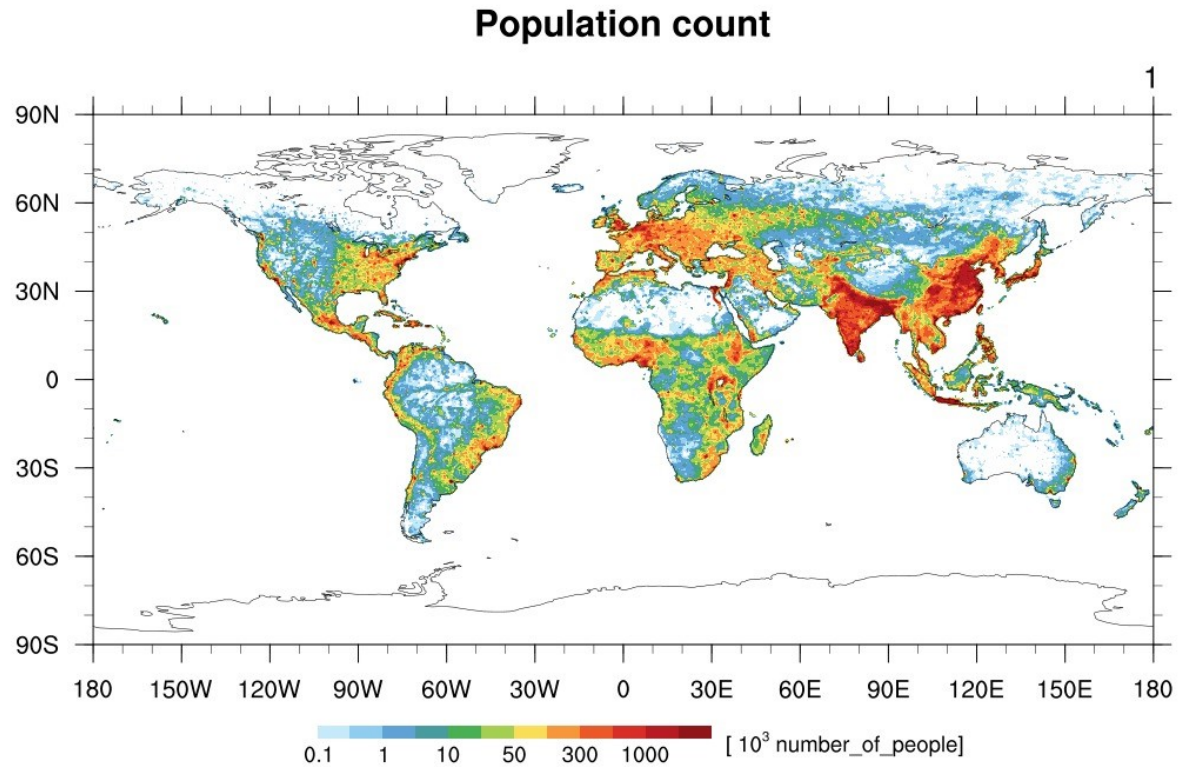

Figure S16. Global population distribution represented as a colour map, indicating population density across different regions of the world.

Table S1. Comparative performance of the $CaCl_2$@GAS composite sorbent with previously reported composite sorbents.

Salt	Supporting Matrix	Sorption T (°C)	Sorption RH (%)	Sorption Capacity (g/g)	Energy density (kJ/kg)	Ref
LiCl	SG	35	15	0.2	1159	[6]
$CaCl_2$	SG	20	30	0.27	746	[7]
$CaCl_2$	Al2O3	20	30	0.17	576	[7]
$CaCl_2$	Bentonite	20	30	0.23	719	[7]
$CaCl_2$	GA	30	30	0.76	1841	[8]
$CaCl_2$	Alginate	30	30	0.88	1206	[9]
$CaCl_2$	MIL 101(Cr)	30	30	0.58	1746	[10]
LiCl	GAF	25	30	0.66	…	[11]
$CaCl_2$	GAS	25	30	0.85	2280	This work
$CaCl_2$	GAS	25	50	1.28	3418	This work
$MgSO_4$	Zeolite	20	56	….	1127	[12]
LiCl	GAF	25	60	1.4	…	[11]
$CaCl_2$	GAS	25	60	1.93	4987	This work
$CaCl_2$	GAS	25	70	2.29	6155	This work
$CaCl_2$	GAS	25	80	2.80	7443	This work
LiCl	P(SBMA-co-AM)	30	80	4.51	9759	[13]
$MgSO_4$	Vermiculite	23	95	….	407	[14]
$CaCl_2$	UiO-66	25	90	1.86	3056	[15]

$CaCl_2$	GA	30	90	2.89	7768	[8]
LiCl	GAF	25	90	4.14	6930	[11]
$CaCl_2$	GAS	25	90	3.96	10426	This work

Table S2. Temperature-dependent EV driving range and relative range reduction derived from real-world driving dataset (345,622 trips).[16] Driving range at 21–25 °C is defined as the

baseline (100%). The “driving range increase (%)” corresponds to the estimated recoverable range fraction if HVAC/BTM energy demand is supplied by the e-thermal bank (i.e., mitigating temperature-induced range loss).

Ambient Temperature (◦C)	**Number of Trips**	**Driving range (km)**	**Driving range increase (%)**
-21 to -20	3	57.702	82.03544
-19 to -15	28	110.271	65.66895
-14 to-10	82	97.688	69.58646
-9 to -5	159	192.310	40.12746
-4 to 0	422	254.061	20.90231
1 to 5	1659	289.501	9.86865
6 to 10	9380	268.258	16.48231
11 to 15	25,247	289.526	9.86087
16 to 20	43,911	309.829	3.53986
21 to 25	48,374	321.199	0
26 to 30	51,920	319.515	0.52429
31 to 35	61,461	308.847	3.84559
36 to 40	59,230	292.224	9.02089
41 to 45	37,356	265.219	17.42845
46 to 50	6311	232.481	27.62088
51 to 53	79	223.379	30.45464

References

1. C. Y. Wang, G. Zhang, S. Ge, T. Xu, Y. Ji, X. G. Yang and Y. Leng, *Nature*, 2016, **529**, 515-518.

2. Y. Zeng, B. Zhang, Y. Fu, F. Shen, Q. Zheng, D. Chalise, R. Miao, S. Kaur, S. D. Lubner, M. C. Tucker, V. Battaglia, C. Dames and R. S. Prasher, *Nat Commun*, 2023, **14**, 3229.
3. M. Hao, J. Li, S. Park, S. Moura and C. Dames, *Nat. Energy*, 2018, **3**, 899-906.
4. N. Javani, I. Dincer and G. F. Naterer, *Energy*, 2012, **46**, 109-116.
5. D. Peng, G. U. Xiaoyonga, W. Ying, X. Jiacheng, S. Mengqiang and L. I. Kaiyun, *Appl. Therm. Eng.*, 2023, **235**.
6. N. Yu, R. Z. Wang, Z. S. Lu and L. W. Wang, *Chem. Eng. Sci.*, 2014, **111**, 73-84.
7. A. Jabbari-Hichri, S. Bennici and A. Auroux, *Sol. Energy Mater. Sol. Cells*, 2017, **172**, 177-185.
8. T. Yan, T. Li, J. Xu, J. Chao, R. Wang, Y. I. Aristov, L. G. Gordeeva, P. Dutta and S. S. Murthy, *ACS Energy Letters*, 2021, **6**, 1795-1802.
9. P. A. Kallenberger, K. Posern, K. Linnow, F. J. Brieler, M. Steiger and M. Fröba, *Advanced Sustainable Systems*, 2018, **2**.
10. A. Permyakova, S. Wang, E. Courbon, F. Nouar, N. Heymans, P. D'Ans, N. Barrier, P. Billemont, G. De Weireld, N. Steunou, M. Frère and C. Serre, *J. Mater. Chem. A*, 2017, **5**, 12889-12898.
11. Y. Hou, Z. Sheng, C. Fu, J. Kong and X. Zhang, *Nat Commun*, 2022, **13**, 1227.
12. G. Whiting, D. Grondin, S. Bennici and A. Auroux, *Sol. Energy Mater. Sol. Cells*, 2013, **112**, 112-119.
13. H. Shan, Z. Zeng, X. Yang, P. Poredoš, J. Yu, Z. Chen and R. Wang, *ACS Energy Letters*, 2023, **8**, 5184-5191.
14. S. P. Casey, J. Elvins, S. Riffat and A. Robinson, *Energy and Buildings*, 2014, **84**, 412-425.
15. L. Garzón-Tovar, J. Pérez-Carvajal, I. Imaz and D. Maspoch, *Adv. Funct. Mater.*, 2017, **27**.
16. N. C. Parker, M. Kuby, J. Liu and E. B. Stechel, *Applied Energy*, 2025, **380**.